Research Article

Nano Research
2021, 14(8): 2558–2567

ISSN 1998-0124 CN 11-5974/O4
https://doi.org/10.1007/s12274-020-3252-4

Lattice-strained nanotubes facilitate efficient natural sunlight-driven CO_2 photoreduction

Shujie Liang[1,§], Xueming Liu[1,§], Zuqi Zhong[1], Bin Han[1], Xiaohui Zhong[1], Weiyi Chen[1], Kainan Song[1], Hong Deng[1,2] (✉), and Zhang Lin[1,2]

[1] *School of Environment and Energy, Guangdong Provincial Key Laboratory of Solid Wastes Pollution Control and Recycling, South China University of Technology, Guangzhou 510006, China*

[2] *Guangdong Engineering and Technology Research Center for Environmental Nanomaterials, The Key Laboratory of Pollution Control and Ecosystem Restoration in Industry Clusters (Ministry of Education), Guangzhou 510006, China*

[§] *Shujie Liang and Xueming Liu contributed equally to this work.*

Received: 22 September 2020 / **Revised:** 16 November 2020 / **Accepted:** 19 November 2020

ABSTRACT

Photocatalytic reduction of CO_2 holds tremendous promise for alleviating the energy crisis. Despite the progress that has been made, there are still some challenges to overcome, such as the realization under real sunlight rather than the simulation condition. In this work, ultrathin $Ni_2(OH)(PO_4)$ nanotubes (NTs) prepared through hydrothermal route are applied as a novel catalyst for photocatalytic reduction of CO_2 under real sunlight. The prepared $Ni_2(OH)(PO_4)$ NTs exhibit a 11.3 μmol·h^{-1} CO production rate with 96.1% CO selectivity. Interestingly, $Ni_2(OH)(PO_4)$ NTs have a positive impact on the facilitation of photoreduction in diluted CO_2. Notably, when the system is performed under real sunlight, $Ni_2(OH)(PO_4)$ NTs afford an accumulated CO of ca. 26.8 μmol with 96.9% CO selectivity, exceeding most previous inorganic catalysts under simulated irradiation in the laboratory. Our experimental results demonstrate that the multisynergetic effects induced by surface-OH and the lattice strain serve as highly active sites for CO_2 molecular adsorption and activation as well as electron transfer, hence enhancing photoreduction activity. Therefore, this work provides experimental basis that CO_2 photocatalysis can be put into practical use.

KEYWORDS

CO_2 photoreduction, diluted CO_2, lattice strain, natural sunlight, application

1 Introduction

Heavy reliance on fossil fuels results in ever-increasing CO_2 emission and then causes energy crisis and global environmental burden [1]. Converting the "waste" CO_2 into valuable chemicals by the photocatalytic process shows great promise for simultaneously alleviating energy and environmental troubles [2, 3]. Despite the progress that has been made, there are still some challenges to overcome. Firstly, the CO_2 conversion efficiency is still fairly low due to their thermodynamical stability with high dissociation energy of the C=O bond (ca. ~ 750 kJ·mol^{-1}) [4]. Then, the sluggish kinetic process with multielectron reaction and protons transfer process greatly impede the selectivity of a specific product among many possible reaction species [5]. Moreover, most works require high purity gases for facilitating CO_2 adsorption and activation [6]. In this case, utilizing a low concentration of CO_2 directly by photocatalysis could be a promising energy-saving method [7]. Last but not least, low conversion efficiency and the required special devices during the CO_2 process keep photoreduction still away from practical application [8]. Therefore, to realize the effective adsorption and activation of CO_2 on the surface of photocatalyst is vital to improve photocatalytic performance and expand application fields.

In order to improve the efficiency of CO_2 photoconversion, various technical approaches have been developed, such as defect engineering [9], surface plasmon resonance [10], and heterostructure [11]. Among these techniques, lattice strain is a novel and efficient alternative to adjust the intrinsic mechanical and electronic properties for tailoring the reactivity [12]. Despite their high efficiency, there are some limitations during the preparation which restrict their further use. Firstly, the surface strain is imposed by external stress from a heterogeneous substrate, which is a complex and time-consuming process [13]. Secondly, the lattice-strained catalytic reactions usually occur at the interface between different crystalline components, where the strain will decay and relax away from the interface [14]. Thirdly, it may be difficult to distinguish the strain effect from interfacial reconstructions, nano-effects, and other factors [15]. In addition, earlier studies mainly focused on the relationship between electrocatalytic activity and strain effect; many other potential applications can be pursued across photocatalysis [12]. To the best of our knowledge, there is no corresponding report about CO_2 photoreduction relative to lattice strain, not to mention the diluted CO_2. To get into the relationship between lattice strain and CO_2 photoreduction, it is crucial to establish a simple and well-defined system with a precise strain generation strategy.

To address the problem discussed above, lattice strain on the surface of circular substrate is anticipated. Interestingly,

Address correspondence to dengh2016@scut.edu.cn

when a thin film bonded to the surface of a circular substrate, the consequent curvature of the substrate could induce mismatch strain and then lattice strain in the film [16, 17]. Nanotubes can be viewed as a flexible two-dimensional (2D) material that is rolled up into a nanoscale tube structure [18]. So, as 2D nanosheets with atomic wavelength scales are sensitive to strain, the twisted surfaces of nanotubes with larger curvature can regulate chemical structure by strain effect to optimize the catalytic performance. Additionally, it is found that strain energy exists on the surface of the nanotube, and it greatly relies on the tube radius in comparison to the 2D nanomaterials [19, 20]. For example, tensile strain on the surface of Pd icosahedra could boost the catalytic activity by shifting up the d-band center and strengthening the adsorption of key intermediate COOH* [21]. Therefore, nanotubes with well-defined strain may be brilliant candidates for the identification of the strain-activity correlation.

Herein, ultrathin $Ni_2(OH)(PO_4)$ nanotubes (NTs) with fewer layers are prepared through a convenient hydrothermal route. The prepared $Ni_2(OH)(PO_4)$ NTs have a clear curved surface with curvature, leading to obvious tensile surface stresses. Significantly, this clear and simple tensile strain on the surface of the tubes is independent of the curved substrate and other special techniques, which can be conducive to a comprehensive understanding of CO_2 photocatalytic process and lattice strain. Experimental results disclose that tensile strain on the surface of the $Ni_2(OH)(PO_4)$ NTs can result in lattice mismatch, and then supply coordinately unsaturated sites to serve as highly active sites (Ni-sites) for CO_2 molecular adsorptions and activation. Meanwhile, the tensile stress can facilitate the electron transfer from the active sites to adsorbed CO_2 molecules on the strained surface. It is worth noting that the hydroxyl group anchoring on the surface can also improve the photoreduction process by coordinating with CO_2 molecular. In conclusion, the multisynergetic effects induced by surface-OH and the lattice strain enable a substantially enhanced performance for CO_2 photocatalysis. Our work will provide an accessible way for the rational design of high-efficiency photocatalytic systems in terms of the lattice strain.

2 Experimental

2.1 Materials

Nickel chloride hexahydrate ($NiCl_2{\cdot}6H_2O$), H_3PO_4 (85 wt.%), dimethylformamide (DMF), $[Ru(bpy)_3]Cl_2{\cdot}6H_2O$ (bpy=2'2-bipyridine), and ethanol were purchased from Sinopharm Chemical Reagent Co., Ltd. (Shanghai, China). The deionized water (18 MΩ· cm) used in all the experiments was prepared by passing through an ultrapure purification system.

2.2 Synthesis of materials

2.2.1 *Synthesis of $Ni_2(OH)(PO_4)$ NTs*

$Ni_2(OH)(PO_4)$ NTs were synthesized by the reported method with slight modification [22]. 0.5 mmol $NiCl_2{\cdot}6H_2O$ was added to a 50 mL Teflon-lined autoclave. Then, 25 mL of DMF and 10 mL of deionized water were added in sequence, and the mixture was stirring for 15 min under room temperature to form a light-green solution. After that, about 34 μL H_3PO_4 (85 wt.%) was added to the above solution, and stirred for another 15 min to get a homogeneous mixture. The autoclave was then heated to 140 °C and maintained for 32 h. After cooling to room temperature, the precipitates obtained were centrifuged, washed with ethyl alcohol several times, and vacuum freeze-drying for 12 h to obtain a pale green precipitate $Ni_2(OH)(PO_4)$ NTs.

2.2.2 *Synthesis of $Ni_2(OH)(PO_4)$ bulks*

$Ni_2(OH)(PO_4)$ bulks were synthesized by the way similar to the above process except the reaction temperature, which was 80 °C here.

2.2.3 *Synthesis of $Ni_3(PO_4)_2$ bulks*

For the preparation of $Ni_3(PO_4)_2$ bulks, 0.291 g $NiCl_2{\cdot}6H_2O$ and 0.110 g sodium phosphate anhydrous were dissolved into 50 mL H_2O, respectively, to get a transparent solution. Then, the above solutions were mixed at room temperature and stirred for 30 min, then kept still for 6 h. After that, the obtained precipitates were washed several times by deionized water and ethanol, and vacuum freeze-drying for 12 h.

2.3 Material characterization

X-ray diffraction (XRD) patterns were recorded by a Bruker D8 Advance Powder X-ray diffractometer with Cu Kα radiation (λ = 1.54178 Å) from 10° to 80° with scan rate of 0.02° per second under normal condition (40 kV, 40 mA). The field emission scanning electron microscopy (FE-SEM) images were characterized by HITACHI SU-8100 field emission scanning electron microscopy equipped with an X-ray energy-dispersive spectrometer (EDS). Transmission electron microscopy (TEM) images and high-resolution transmission electron microscopy (HRTEM) images were operated by JEOL model JEM 2010 EX instrument at an acceleration voltage of 200 kV. X-ray photoelectron spectroscopy (XPS) measurements were performed using a Thermo Scientific ESCA Lab250 spectrometer by referencing C 1s to 284.6 eV. The photoluminescence (PL) spectra were investigated on an Edinburgh FL/FS900 spectrophotometer. The Fourier transformed infrared spectroscopy (FT-IR) was conducted in a Nicolet Nexus 670 FT-IR spectrophotometer from 400 to 4,000 cm^{-1} region at a resolution of 4 cm^{-1}. Micromeritics ASAP 2020 analyzer are used to get the information of Brunauer-Emmett-Teller (BET) surface area and porous structure by N_2 adsorption/desorption isotherms method. Additionally, the CO_2 adsorption isotherms were analyzed using a Micromeritics ASAP 2020 analyzer at 298 K. All of the samples were degassed before the sorption measurements. Photocatalysis tests were put in the PCX50B Discover multi-channel parallel photocatalytic reaction system (Perfect Light Co., Ltd.) with a 5 W white LED light (400 nm ≤ λ ≤ 800 nm). The photoreduction products were determined and quantified by gas chromatography (GC-7890B, Agilent). $^{13}CO_2$ isotopic experiment and its reaction products were conducted by GC-MS system (Agilent 7890B-5977A).

2.4 X-ray absorption spectroscopy (XAS) spectra collection and analysis

A certain amount of sample was pressed into circular pellets with a diameter of 10 mm for further extended X-ray absorption fine structure (EXAFS) measurement. Raw XAS data were obtained from the Beijing Synchrotron Radiation Facility at 1W1B, Institute of High Energy Physics, Chinese Academy of Sciences. The storage ring energy is 2.5 GeV with current between 160 and 250 mA under ambient conditions. Ni K-edge EXAFS was collected by transmission mode with appropriate absorption edge jump in the range from 8,137 to 9,122 eV with a step-size of 0.7 eV at the near edge. The acquired raw data were processed through standard procedures with energy calibration, data alignment, background subtraction, normalization, and Fourier transformation by the ATHENA and ATHENA program in IFEFFIT software [23].

2.5 Photocatalytic CO_2 reduction process

Photocatalytic CO_2 process was conducted in a liquid-solid reaction system by a multi-channel parallel photocatalytic reaction system. A certain amount of catalyst, 7.5 mg $[Ru(bpy)_3]Cl_2{\cdot}6H_2O$ (abbreviated as Ru) and 6 mL mixed MeCN/H_2O/TEOA solution (v/v/v: 3/2/1) were added in a 60 mL gas-closed quartz reactor. Then the reactor was evacuated by a mechanical pump, and then purged with CO_2 of a certain concentration. This process would be repeated three times in order to fully remove the dissolved air. Then, the reactor was put in a PCX50B Discover multi-channel parallel photocatalytic reaction system (Perfect Light Co., Ltd.) with a 5 W white LED light (400 nm ≤ λ ≤ 800 nm) at ambient temperature under atmospheric pressure with continuous magnetic stirring. And the gas product was analyzed by gas chromatography (GC-7890B, Agilent). During the reaction process, the photocatalytic system was kept at constant room temperature by electronic fans.

The selectivity for CO was calculated using the equation below

$$\text{Selectivity of CO} = n(\text{CO})/[n(\text{CO})+n(\text{H}_2)] \times 100\%$$

3 Results and discussion

$Ni_2(OH)(PO_4)$ NTs were fabricated through a convenient hydrothermal method in the mixed DMF/H_2O solvent (Scheme 1), and the detailed preparation is listed in the experimental section. The morphology of the $Ni_2(OH)(PO_4)$ NTs was characterized by FE-SEM. As shown in Fig. S1(a) in the Electronic Supplementary Material (ESM), the low-magnification FE-SEM image indicates that the typical product consists of a large number of uniform microspheres. Figure S1(b) in the ESM shows the single microsphere of $Ni_2(OH)(PO_4)$ NTs, which has cotton candy-like nanostructures. Figure 1(a) shows an enlarged FE-SEM image of some representative area indicates that the interior of the microspheres is composed of one-dimensional ultrathin nanostructures. TEM observations further confirms the result of the SEM. As shown in Fig. 1(b), the TEM images indicate that the obtained nanotubes are highly uniform with a length of about 5 μm. A high-magnification TEM image reveals that the diameter of the nanotube is about 5 nm with a small hollow center and several walls (Fig. 1(c)). And the morphology of its bulk contrast sample, $Ni_2(OH)(PO_4)$ bulk and $Ni_3(PO_4)_2$ bulk, is also shown in Fig. S2 in the ESM. Clearly, the ultrathin nanotubes are interwoven with each other and form well-defined cotton candy-like nanostructures.

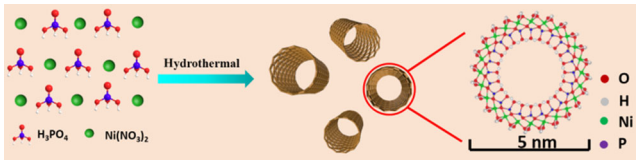

Scheme 1 Schematic illustration of the synthesis of $Ni_2(OH)(PO_4)$ NTs.

The crystal structures of the as-obtained $Ni_2(OH)(PO_4)$ NTs were characterized by XRD. As shown in Fig. 1(d), the XRD diffraction peaks are low and broad, revealing poor crystallinity nature out of the ultrathin nanostructure. The composition of ultrathin $Ni_2(OH)(PO_4)$ NTs has been determined by EDS. As shown in Fig. 1(e), the energy-dispersive spectroscopy demonstrates there are mainly three kinds of elements in $Ni_2(OH)(PO_4)$ NTs, including Ni, O, P. The element distribution of $Ni_2(OH)(PO_4)$ NTs has been characterized by EDS elemental mapping. Ni, P, and O are all uniformly distributed along the entire $Ni_2(OH)(PO_4)$ NTs (Fig. 1(f)). The FT-IR analysis provides important molecular structural information. As shown in Fig. S3(a) in the ESM, the obvious peaks at 1,021 and 575 cm^{-1} are related to PO_4 and Ni-O, respectively. The predominant overlapped absorption band from 3,000 to 3,700 cm^{-1} is assigned to the v(O–H) stretching mode of surface hydroxyl groups or adsorbed water, respectively. Thermogravimetric analysis (TGA) shows the multistep weight loss when the temperature rises from 25 to 800 °C (Fig. S3(b) in the ESM). By analyzing the results of the TGA, we find that the mass of the samples decreased by about 28%. It is noted that during thermal decomposition, $Ni_2(OH)(PO_4)$ NTs underwent two obvious processes of mass losses. The first rapid step occurs at nearly 230 °C with about 19 wt.% of mass loss due to the removal of adsorbed water on the surface. As for the second step, about 9 wt.% weight loss is observed during the heating-up process from 230 to 600 °C, which can be ascribed to the decomposition of the hydroxyl group of the obtained $Ni_2(OH)(PO_4)$ NTs [22]. From the above analysis, it is concluded that there are plenty of hydroxyl groups in the $Ni_2(OH)(PO_4)$

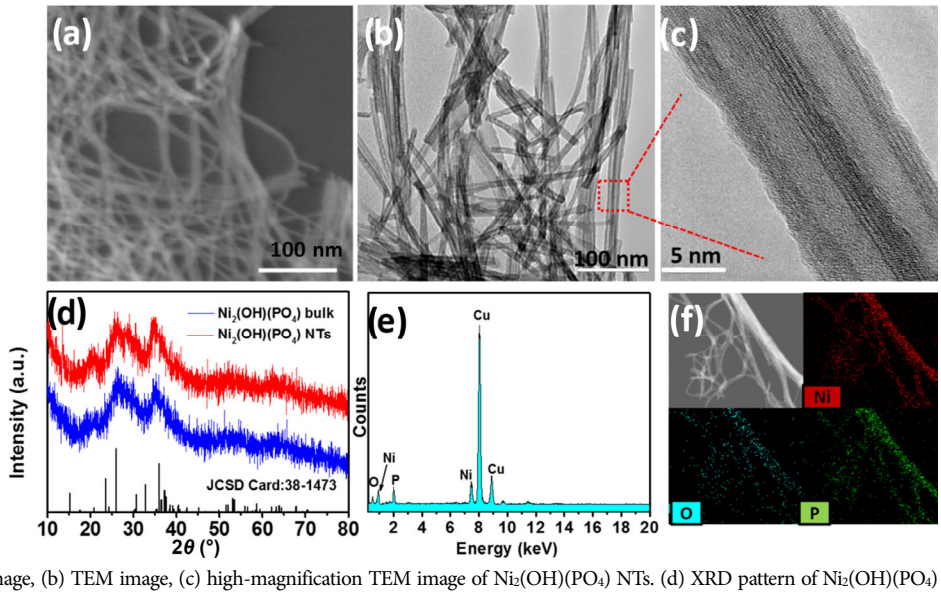

Figure 1 (a) SEM image, (b) TEM image, (c) high-magnification TEM image of $Ni_2(OH)(PO_4)$ NTs. (d) XRD pattern of $Ni_2(OH)(PO_4)$ NTs and bulk. (e) EDX spectrum, and (f) related HAADF-STEM image and EDX elemental mappings of Ni, O, and P in $Ni_2(OH)(PO_4)$ NTs.

NTs structure.

XPS confirmed the composition and chemical state of the $Ni_2(OH)(PO_4)$ NTs, with binding energy for the C 1s peak (284.6 eV) utilized as an internal reference. The XPS survey spectrum shows the existence of elements Ni, P, and O (Fig. S4 in the ESM). The atomic percentages of Ni, P, and O on the surface of $Ni_2(OH)(PO_4)$ NTs are found to be around 12.52%, 10.6%, and 52.08%, respectively. No specific peaks of nitrogen have been found at 398.2 eV, indicating no DMF remaining in the structure of $Ni_2(OH)(PO_4)$ NTs. The Ni 2p XPS spectra are fitted with four peaks at 855.58, 861.36, 873.39, and 879.38 eV, respectively (Fig. 2(a)). The peaks occurring at around 855.58 and 861.36 eV can be in accordance with the binding energies of Ni 2p3/2, and the peaks at 873.39 and 879.38 eV can be assigned to Ni 2p1/2 [24, 25]. Additionally, the high-resolution spectra for the O 1s region shows three oxygen contributions (Fig. 2(b)). The fitting peak at 529.8 eV is deemed as oxygen bond of Ni–O. The component located at 531.4 eV corresponds to plenty of defect sites with low oxygen coordination, which can be observed usually in materials with ultrathin nanostructures [26]. Moreover, the component at 532.33 eV can be assigned to surficial hydroxyl, indicating there are plenty of surficial hydroxyl on the surface of the prepared $Ni_2(OH)(PO_4)$ samples, which is corresponding to the TGA results. So, the XPS data clearly demonstrate that the as-prepared $Ni_2(OH)(PO_4)$ NTs have numerous hydroxyl groups on the surface.

The X-ray absorption near-edge spectroscopy (XANES) and EXAFS are effective characterization techniques for monitoring the electronic and coordination structures of the catalyst. Three different samples of $Ni_2(OH)(PO_4)$ NTs, $Ni_2(OH)(PO_4)$ bulk, and $Ni_3(PO_4)_2$ bulk show similar patterns in Ni K-edge XANES spectra (Fig. 2(c)), indicating the $Ni_2(OH)(PO_4)$ NTs and bulk keep similar microstructure with $Ni_3(PO_4)_2$ bulk. In addition, as shown in Fig. S5 in the ESM, the $Ni_2(OH)(PO_4)$ NTs and their bulk counterparts exhibit similar Ni K-edge oscillation curves, further suggesting their same configuration of Ni–O coordination. The white line intensities in the normalized XANES spectra are proportional to the oxidation states of Ni and manifests the electronic density of unoccupied d states. As shown in Ni K-edge XANES profiles, the white line intensity of $Ni_2(OH)(PO_4)$ NTs is higher than that of the Ni foils, indicating the chemical state of Ni is mainly 2+ in the $Ni_2(OH)(PO_4)$ NTs, which is in agreement with the XPS results. Compared with $Ni_2(OH)(PO_4)$ bulk, the white line intensity of $Ni_2(OH)(PO_4)$ NTs shows a much lower value, indicating the structure of the nanotubes could transfer electron to Ni atom [27]. Fourier transform EXAFS spectroscopy in *R* space (Fig. 2(d)) shows primary peaks located at ~ 1.60 and 2.67 Å, corresponding to the Ni–O and Ni–Ni scattering path, respectively. Notably, the first shell signal of the Ni–O bond and the second core-shell peak of the Ni–Ni from the $Ni_2(OH)(PO_4)$ NTs clearly shift to a lower *R* compared with that of $Ni_2(OH)(PO_4)$ bulks and $Ni_3(PO_4)$ bulks, indicating the significant change in the microstructure of the nanotubes. Then, the EXAFS spectra at the Ni K-edge and the corresponding fitting results are summarized in Fig. S6 and Table S1 in the ESM. According to the first-shell fitting analysis of the Ni K-edge (Table S1 in the ESM), a coordination number of ~ 6.0 is observed for the Ni–O coordination sphere, which is in agreement with the octahedral-hexacoordinated structure (NiO_6) in the $Ni_2(OH)(PO_4)$ nanotubes and $Ni_2(OH)(PO_4)$ bulks. Moreover, the average bond length of Ni–O decreased from 2.06 Å in the $Ni_2(OH)(PO_4)$ bulks to 2.05 Å in the $Ni_2(OH)(PO_4)$ NTs. This result indicates that the curved surface makes for lattice distortion, then causing the lattice strain of the crystallographic unit cell. In all, the formation of lattice strain on the surface of the nanotubes structure is successfully validated, and the following photoreduction may be anticipated.

The photocatalytic CO_2 reduction performance of the $Ni_2(OH)(PO_4)$ NTs was investigated in a mild catalytic system carried out in H_2O/acetonitrile mixture under visible light irradiation, with $Ru(bpy)_3^{2+}$ and triethanolamine (TEOA) as the photosenitizer and electron donor, respectively. The photocatalytic processes with different amount of $Ni_2(OH)(PO_4)$ NTs catalysts were firstly tested to evaluate the photocatalytic performance. As shown in Fig. 3(a), the amount of $Ni_2(OH)(PO_4)$ NTs catalysts plays an important role in the whole catalytic process, especially in the production yield. Generally, CO was detected to be the major gaseous product accompanied by tiny H_2 as the byproduct, and no liquid products were found. As we can see, the photocatalytic activities and selectivity of these samples have an increasing volcanic type trend with the input amount of the $Ni_2(OH)(PO_4)$ NTs; and when the input

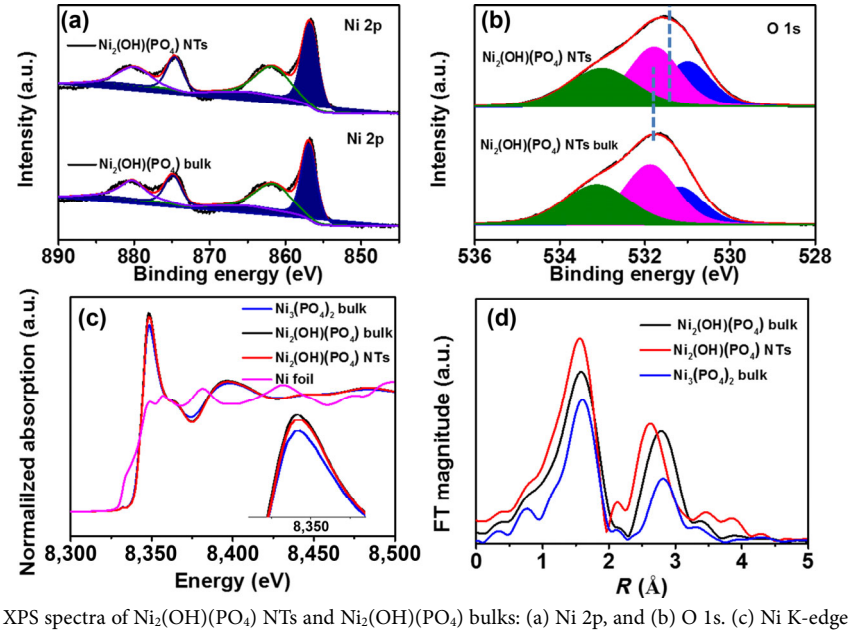

Figure 2 High resolution XPS spectra of $Ni_2(OH)(PO_4)$ NTs and $Ni_2(OH)(PO_4)$ bulks: (a) Ni 2p, and (b) O 1s. (c) Ni K-edge XANES spectra and (d) its corresponding Fourier transform magnitudes of k^2-weighted EXAFS spectra.

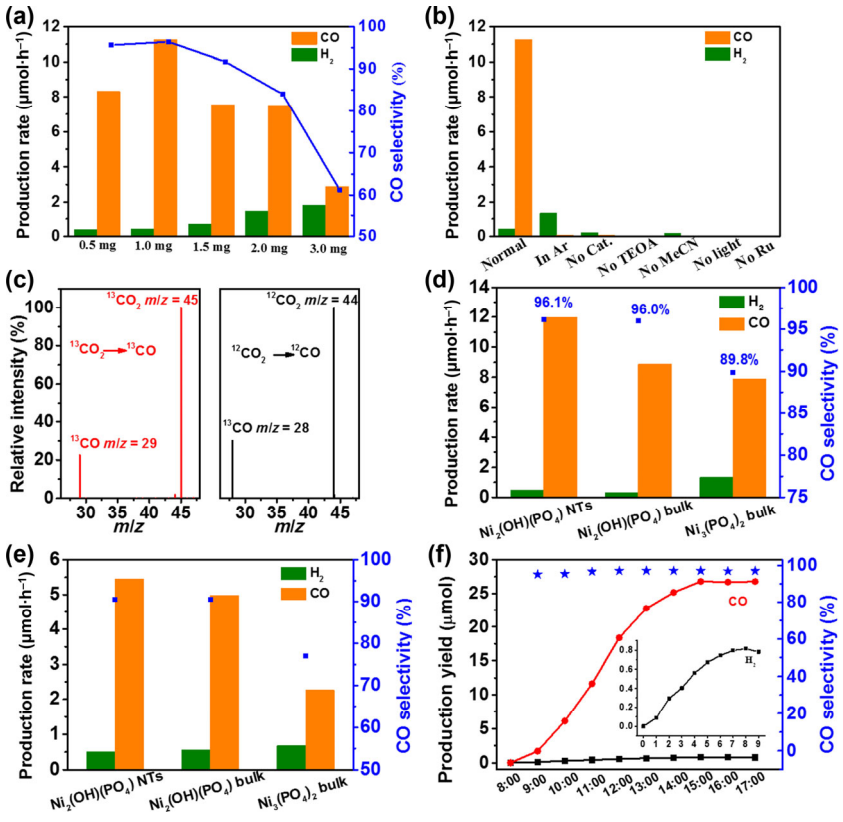

Figure 3 (a) Photocatalytic production rate and selectivity of CO by different quality of catalyst. (b) Photocatalytic evolution of CO and H_2 under various reaction conditions. (c) The isotope analysis of CO using $^{13}CO_2$ and $^{12}CO_2$ as carbon source by GC-MS. Photocatalytic performance in (d) pure, and (e) diluted CO_2. (f) Sunlight-driven CO_2 reduction in 9 h.

quantity of $Ni_2(OH)(PO_4)$ NTs increased to 1 mg, the system shows the most prominent activity with CO evolution up to 11.3 μmol·h^{-1} and CO selectivity to 96.1%. However, when the added amount of $Ni_2(OH)(PO_4)$ NTs catalysts is below or above 1 mg, obviously decreased CO evolution rate and selectivity could be observed. The number of catalytic sites participating in the catalytic reaction and the ability to accept excitation light are main reasons for this phenomenon. When the catalyst content is low, the sites involved in the catalytic reaction are few, thereby resulting in low catalytic activity. As the catalyst content increases, the number of catalytic sites involved gradually increases, so does the catalytic activity. However, when the catalyst content is too high, it will weaken the ability of the photosensitizer to receive visible light radiation, resulting in a decrease in catalytic activity [2, 28, 29]. Furthermore, the $Ni_2(OH)(PO_4)$ NTs keep constant CO evolution rates within the total reaction process, implying the high stability of the photocatalyst (Fig. S7 in the ESM). Therefore, 1 mg of the catalyst exhibited the best performance in photocatalysis and was used in subsequent experiments.

To better elucidate the essence of the photocatalysis reaction, a series of control experiments have been conducted (Fig. 3(b)). As presented in Fig. 3(b), column 2, when Ar is used instead of CO_2 to carry out the reaction under the identical condition, only a small amount of H_2 is generated without any evolution of CO, clearly indicating that the CO product indeed originates from the splitting of CO_2 molecules. Compared with the normal tests (Fig. 3(b), column 1), when there is no $Ni_2(OH)(PO_4)$ NTs catalyst in the system, a slight amount of H_2 is generated, and almost no CO is produced (Fig. 3(b), column 3), indicating that $Ni_2(OH)(PO_4)$ NTs play an important role in our catalytic reaction. A comparative test is performed with no TEOA added, negligible amounts of CO and H_2 are detected (Fig. 3(b), column 4), highlighting the crucial role of electron donor during the reaction process. As a comparison, in the absence of MeCN (Fig. 3(b), column 5), the CO production is significantly suppressed, indicating that MeCN promotes the reduction reaction of CO_2 by increasing the dissolution of CO_2. Experiments carried out in the absence of Ru or visible light irradiation, as revealed in Fig. 3(b), columns 6 and 7, indicating that the reaction is driven by the harvested light photons of Ru. Besides, as shown in Fig. S8 in the ESM, the tendency of CO production considerably coincides with the absorption spectrum of the Ru complex, further indicating that the CO_2-to-CO conversion was initiated from light radiation [30].

In order to further confirm the origin of the CO, isotopetracing experiments were conducted, and the gas-products were identified by gas chromatography mass spectrometry (GC-MS). As shown in Fig. 3(c), with $^{12}CO_2$ as feedstock gas for the photoreduction, the major mass/charge ratio peak at 28 can correspond to the ^{12}CO products. Furthermore, the $^{13}CO_2$ labeling experiments generate an obvious signal at 29 instead of 28, strongly referring to ^{13}CO. These results unambiguously indicate that CO formation originated from the photocatalytic reduction of CO_2 over $Ni_2(OH)(PO_4)$ NTs under visible-light irradiation, rather than the decomposition of the organic matter in the reduction system or the pollution from other carbon sources.

Catalytic performances of the three catalysts were firstly evaluated in the pure CO_2 under the optimal laboratory condition. As shown in Fig. 3(d), $Ni_2(OH)(PO_4)$ NTs exhibit about 11.3 μmol·h^{-1} CO production rate with 96.1% CO selectivity, and the catalytic selectivity is the best based on a summary of the visible-light-driven inorganic catalysts (Table S2 in the ESM). Although there is no significant change in the CO selectivity, the CO production rate of $Ni_2(OH)(PO_4)$ bulk decreases to 8.87 μmol·h^{-1} compared with $Ni_2(OH)(PO_4)$ NTs.

Meanwhile, when it comes to $Ni_3(PO_4)_2$ bulks, the CO activity and selectivity sharply decrease to 7.90 μmol·h^{-1} and 89.8%, respectively. Obviously, the CO evolution and selectivity of $Ni_2(OH)(PO_4)$ NTs is higher than its comparison of $Ni_2(OH)(PO_4)$ bulk and $Ni_3(PO)_4$ bulks, indicating the $Ni_2(OH)(PO_4)$ NTs with special ultrathin nanotubes show a significant advantage for boosting CO_2 reduction.

Then, the photocatalytic performances of the three samples were further performed in diluted CO_2 at 0.1 atm for 3 h. As shown in Fig. 3(e), $Ni_2(OH)(PO_4)$ NTs show 5.5 μmol·h^{-1} CO production rate with 90.5% CO selectivity in 0.1 atm, which is about 32 times as high as the blank group without catalyst in the pure CO_2, indicating $Ni_2(OH)(PO_4)$ NTs is a kind of effective catalyst to drive the photocatalytic process indiluted CO_2. In the meantime, the catalytic results of $Ni_2(OH)(PO_4)$ bulk and $Ni_3(PO)_4$ bulks are also recorded.

When it comes to $Ni_2(OH)(PO_4)$ bulk in 0.1 atm, the CO production rate and selectivity reach 4.9 μmol·h^{-1} and 90.0%, respectively. As for $Ni_3(PO)_4$ NTs, the catalytic performance of both CO production rate and selectivity is further surpassed $Ni_2(OH)(PO_4)$ bulks, further indicating the advantages of tubular structures and components in $Ni_2(OH)(PO_4)$ NTs. Besides, it is noted that the catalytic activity and selectivity decreased with the reduced CO_2 concentration, which is observed both in all three samples, revealing a direct influence of CO_2 concentration on the catalytic rates and product selectivity.

Moreover, current photocatalytic experiments especially CO_2 reduction were fully completed under simulated conditions in the laboratory, which are far away from actual practice. For practical applications, inadequate catalytic effectiveness and specific complex of the reaction condition are the bottlenecks. In other words, the significant increase of efficiency and the simplicity of manipulations are the crucial factors for transformation from theoretical research to the real application. In our work, $Ni_2(OH)(PO_4)$ NTs with the conspicuous activity of CO_2-to-CO are employed to verify the possibility of practical applications under natural sunlight (Fig. 3(f)). In order to simplify the operations, a simple closed system with static conditions appears to be the preferred protocol approach. The $Ni_2(OH)(PO_4)$ NTs reaction suspension was prepared in a gas-closed quartz reactor without stirring and placed on the roof of the environmental building at South China University of Technology (Fig. S9 in the ESM). This reaction was conducted in a sunny day from 8:00 am to 17:00 on Dec. 26th in 2019. $Ni_2(OH)(PO_4)$ NTs exhibit a nearly linear increase of CO evolution with a little amount of H_2 during the total reaction, affording an accumulated CO of ca. 26.8 μmol with 96.9% CO selectivity, the catalytic selectivity is among the best based on a review of the recent visible-light-driven heterocatalysts which surpasses or is comparable to the simulated results in the laboratory (Table S2 in the ESM); however, with the further extension of the reaction time, the catalytic activity gradually loses, mainly due to the photobleaching of the sensitizer [31–33]. These results not only underline the remarkable CO_2 reduction performance of $Ni_2(OH)(PO_4)$ NTs, but also confirm the possibility of the practical application of photocatalysis.

As is well-known, the photocatalytic reaction is intrinsically governed by charge separation and migration following photo-excitation, thus it is essential to monitor the charge-transfer behavior between catalyst and reactant [34–36]. Therefore, we resorted to the steady-state photoluminescence track charge carrier dynamics during the reaction. As shown in Fig. 4(a), the blank system with only photo-sensitizer Ru shows a

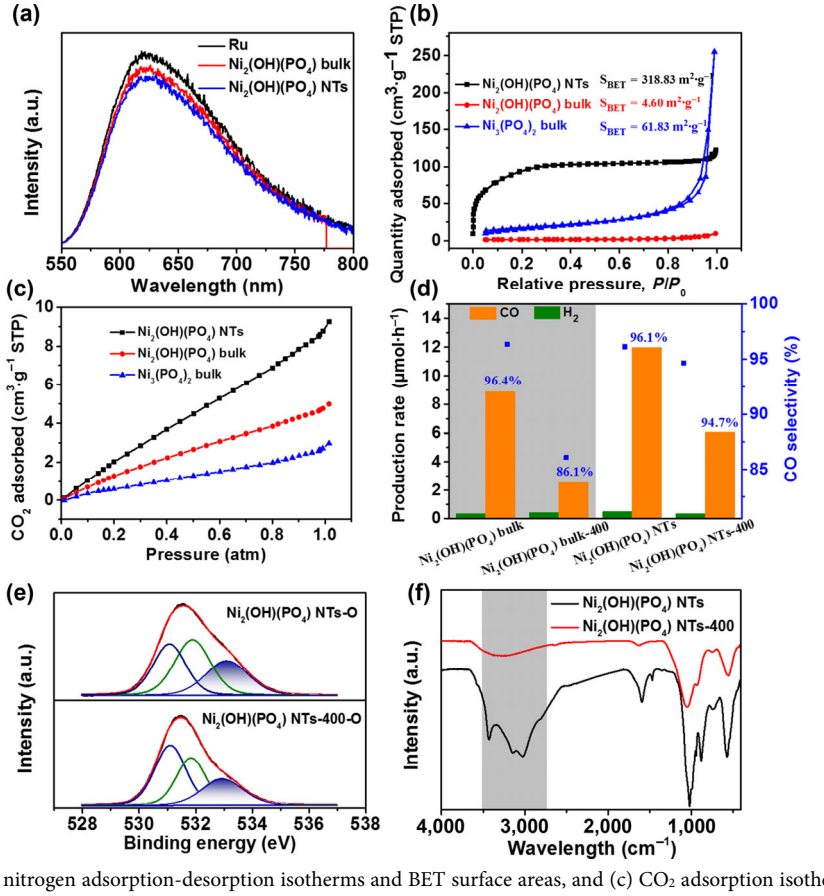

Figure 4 (a) PL spectra, (b) nitrogen adsorption-desorption isotherms and BET surface areas, and (c) CO_2 adsorption isotherm for $Ni_2(OH)(PO_4)$ NTs, $Ni_2(OH)(PO_4)$ bulk, and $Ni_3(PO)_4$ bulks. (d) Comparison of photocatalytic performance over $Ni_2(OH)(PO_4)$ bulk and $Ni_2(OH)(PO_4)$ NTs before and after high temperature calcination. (e) O 1s spectra, and (f) FT-IR spectra of $Ni_2(OH)(PO_4)$ bulk and $Ni_2(OH)(PO_4)$ NTs before and after high temperature calcination.

strong typical emission signal around 625 nm, ascribed to the detrimental electron-hole combination therein which can hardly be utilized for facilitating CO_2 reaction in the solvent [37]. With the addition of $Ni_2(OH)(PO_4)$ bulk, the typical excited peak of the Ru is quenched, which confirms $Ni_2(OH)(PO_4)$ bulk could bring about additional electron-transfer channels to promote the transfer of photoexcited electrons. Furthermore, the intensity of the $Ni_2(OH)(PO_4)$ NTs is even lower than that of $Ni_2(OH)(PO_4)$ bulk, demonstrating nanotube structure will accelerate more photoexcited electrons transfer from Ru to the catalytic sites on the surface of nanotubes compared with that of bulk materials [38]. Electrochemical impedance spectroscopy (EIS) measurements have been carried out to further unveil photogenerated separation efficiency. $Ni_2(OH)(PO_4)$ NTs manifest a much smaller radius than that of $Ni_2(OH)(PO_4)$ bulk (Fig. S10 in the ESM), implying its greatly reduced charge transfer resistance [39, 40]. So, the $Ni_2(OH)(PO_4)$ NTs with special lattice-strained walls, compared with normal $Ni_2(OH)(PO_4)$ bulk materials, achieve enhanced spatial separation of photoexcited charge carriers, thereby suppressing the electron-hole combination, which benefits the whole CO_2 photocatalytic performance.

The N_2 adsorption-desorption measurement was carried out to investigated the specific surface area of the as-prepared samples, as shown in Fig. 4(b). Generally, the specific surface area plays a part in determining the photocatalysis properties of the prepared materials. The isotherm of $Ni_2(OH)(PO_4)$ NTs with the highest specific surface area belongs to the typical type I, indicating its typical microporous structure, which is favorable for the diffusion of reactants and products. Meanwhile, $Ni_2(OH)(PO_4)$ NTs exhibit a high BET specific surface area of 318.3 $m^2 \cdot g^{-1}$, which can expose more active sites for the improvement of catalytic activity. So, the tube-like structure of $Ni_2(OH)(PO_4)$ NTs with the high specific surface area can make a significant contribution to the exposure of active species, and contact between reactant and catalysts during the reaction. Although $Ni_2(OH)(PO_4)$ bulk presents a lower specific surface area (4.60 $m^2 \cdot g^{-1}$) than that of $Ni_3(PO_4)_2$ bulk (61.83 $m^2 \cdot g^{-1}$), it unfolds more prominent catalytic properties (8.87 $\mu mol \cdot h^{-1}$) that of $Ni_3(PO_4)_2$ bulk (7.90 $\mu mol \cdot h^{-1}$); meanwhile, a similar trend of CO production selectivity can be observed between $Ni_2(OH)(PO_4)$ bulk and $Ni_3(PO_4)_2$ bulk (Table 1). These opposite trends between the specific surface area and catalytic activity of $Ni_2(OH)(PO_4)$ bulk and $Ni_3(PO_4)_2$ bulk highlight that specific surface area is an important but not the decisive factor for CO_2 catalytic reaction in our work.

Adsorption and activation of CO_2 are prerequisites for the CO_2 photocatalytic reaction [41]. As shown in Fig. 4(c), $Ni_2(OH)(PO_4)$ NTs exhibit the strongest CO_2 adsorption performance (~ 9.70 $cm^3 \cdot g^{-1}$), superior to their counterparts. The dramatic ability of CO_2 capture renders $Ni_2(OH)(PO_4)$ NTs a suitable material for efficient CO_2-to-CO reduction in pure or diluted CO_2. In addition, the efficiency of CO_2-to-CO reduction is consistently correlated positively with CO_2 uptake amount, indicating the CO_2 adsorption and activation may play a decisive role in CO_2 photoreduction. Interestingly, although $Ni_2(OH)(PO_4)$ bulk has a lower specific surface area compared with $Ni_3(PO_4)_2$ bulk, it shows a higher CO_2 uptake of 5.0 $cm^3 \cdot g^{-1}$, which is nearly 1.8 times as large as the $Ni_3(PO_4)_2$ bulk. The higher CO_2 uptake ability of $Ni_2(OH)(PO_4)$ bulks is derived from hydroxyl groups on the surface, which can act as Lewis basic sites with a relatively strong adsorption capacity of CO_2 [42–44]. Meanwhile, the CO catalytic selectivity is improved, suggesting the surficial OH can partly enhance the CO_2 activation to some extent. From the above analysis, we conclude that $Ni_2(OH)(PO_4)$ with ultrathin nanotubes will translate into a large specific surface area which exposes more hydroxyl groups on the surface of the thin walls, enhancing CO_2 adsorption and activation to improve the catalytic activity and selectivity, respectively.

Table 1 The comparison of three different catalysts with photocatalytic performance, CO_2 uptake amount, and specific area

Catalyst	S_{BET} ($m^2 \cdot g^{-1}$)	CO_2 uptake amount ($cm^3 \cdot g^{-1}$)	CO production rate ($\mu mol \cdot h^{-1}$)	CO selectivity (%)
$Ni_2(OH)(PO_4)$ NTs	318.3	9.70	11.3	96.1
$Ni_2(OH)(PO_4)$ bulk	4.60	5.00	8.87	96.0
$Ni_3(PO_4)_2$ bulk	61.83	2.80	7.90	89.8

In addition, the alkalinity of the surface attracts great attention in the field of photocatalytic CO_2 reduction [45, 46]. The surface OH, which acted as Lewis basic sites with a relatively high adsorption capacity of CO_2, can result in the adsorption-enhanced CO_2 reactions [43, 47]. To determine what role OH might play in the reaction process, we directly compared the catalytic properties before and after calcination. As shown in Fig. 4(d), the $Ni_2(OH)(PO_4)$ NTs exhibit striking activity for CO_2 reduction with a CO generation rate and selectivity of 11.9 $\mu mol \cdot h^{-1}$ and 96.4%, respectively. Once the $Ni_2(OH)(PO_4)$ NTs are calcinated with high temperatures (400 °C), the CO generation rate and selectivity are substantially decreased to 6.1 $\mu mol \cdot h^{-1}$ with 94.7% selectivity. Of interest, a similar phenomenon is observed in $Ni_2(OH)(PO_4)$ bulk materials. $Ni_2(OH)(PO_4)$ bulk shows a CO production rate of 9.2 $\mu mol \cdot h^{-1}$ with a selectivity of 96.4%, which is much higher than that of sample after high temperatures calcination (2.6 $\mu mol \cdot h^{-1}$, 86.1%). In order to further prove the promotion of catalytic property by the surficial OH, XPS and FT-IR are well compared before and after calcination. As shown in Fig. 4(e), the high-resolution spectra for the surficial hydroxyl on the $Ni_2(OH)(PO_4)$ NTs at 532.33 eV obviously decrease compared with the samples after calcination, indicating there is plenty of hydroxyl in the structure of $Ni_2(OH)(PO_4)$ NTs. Then, as shown in Fig. 4(f), the OH stretching vibrations of the $Ni_2(OH)(PO_4)$ NTs were also investigated. The contents of the –OH decreased significantly after the calcined process under high temperature, indicating the hydroxyl decomposed during the thermal process. These decreasing trends of surficial OH after calcination are in line with the deteriorative photocatalytic performance. In addition, similar phenomena could also be observed in $Ni_2(OH)(PO_4)$ bulk before and after calcination (Fig. S11 in the ESM). These results clearly declare that the OH on the surface of the $Ni_2(OH)(PO_4)$ makes for the efficient CO_2 reaction, which can not only enhance the CO production rate, but also significantly improve the selectivity for the product. This indicates that the OH group could serve as active sites to optimize the activation and conversion of the adsorbed CO_2 [48, 49].

Based on the above characterizations and analysis, we propose the rational mechanism of CO_2 reduction with $Ni_2(OH)(PO_4)$ NTs (Scheme 2). Under visible-light irradiation, the photosensitizer $[Ru(bpy)_3]Cl_2$ is firstly excited to the excited state. Then the excited state will be reductively transformed into reduced photosensitizer with the help of sacrificial electron from TEOA. Subsequently, the reduced photosensitizer with the intrinsic reduction ability can timely transfer photogenerated electrons to the catalytic sites on the $Ni_2(OH)(PO_4)$ NTs and suppress the probability of carrier recombination. Finally, the captured photogenerated electrons are available to drive the reductive reaction from CO_2-to-CO. During the catalytic

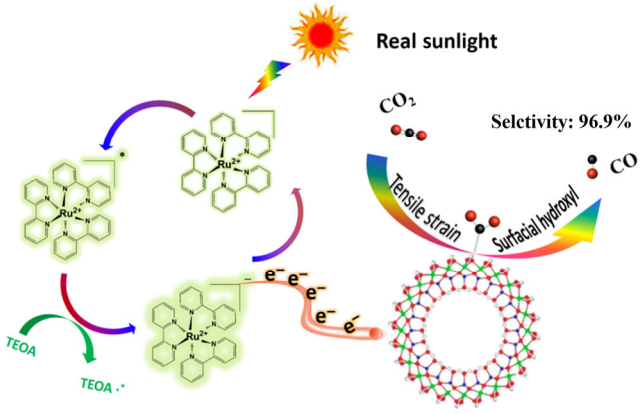

Scheme 2 Proposed reaction pathway of CO formation over the $Ni_2(OH)(PO_4)$ NTs system under natural sunlight irradiation.

process, the protons compete with adsorbed and activated CO_2 on the surface of catalyst for photogenerated electrons from the activated photosensitizer, and the side reaction of hydrogen evolution occurs. In detail, visible-light drives photosensitizer $[Ru(bpy)_3]Cl_2$ to transform into $Ru(bpy)_3^{2+*}$, which keeps strong electron donating ability. The highest occupied molecular orbital (HOMO) of $Ru(bpy)_3^{2+*}$ associated with the delocalized photogenerated electrons from its π* orbital and further transferred to the surface of the $Ni_2(OH)(PO_4)$ NTs [50]. Special ultrathin nanotube structure with large specific surface area can efficiently trap photoexcited electrons from activated sensitizers, which further enhances photocatalysis. In addition, tensile strain not only is a powerful tool for exposing more coordinatively unsaturated Ni sites acted as effective catalytic sites, but also can tune binding affinity of the reactive intermediates, thereby causing an increase in CO_2 photocatalytic activity [51–53]. What's more, OH groups on the surface are vital factors for the overall reaction. On the one hand, OH acted as Lewis basic sites and obtained high adsorption capacity of CO_2 for the adsorption-enhanced CO_2 reactions; on the other hand, OH groups can serve as active sites to stabilize the intermediate adduct and donate a proton to complete the CO_2-to-CO reaction [6]. In this way, the synergy of the tensile strain and surficial OH on $Ni_2(OH)(PO_4)$ NTs are beneficial for the striking CO_2-to-CO photoconversion in diluted CO_2 or in real sunlight conditions.

4 Conclusions

In summary, $Ni_2(OH)(PO_4)$ NTs were fabricated through a convenient hydrothermal method in the mixed DMF/H_2O solvent, and our photocatalytic measurements clearly demonstrate that $Ni_2(OH)(PO_4)$ NTs exhibit a remarkable activity and selectivity towards CO_2. Under the optical conditions, the system of $Ni_2(OH)(PO_4)$ NTs show the most prominent activity with CO evolution up to 11.3 μmol·h^{-1} and CO selectivity to 96.1% in pure CO_2. Furthermore, $Ni_2(OH)(PO_4)$ NTs show 5.5 μmol·h^{-1} CO production rate with 90.5% CO selectivity in 0.1 atm, indicating $Ni_2(OH)(PO_4)$ NTs are effective catalysts to drive the photocatalytic process in diluted CO_2. Most importantly, when the system is conducted under real sunlight irradiation, $Ni_2(OH)(PO_4)$ NTs exhibit a stable increase of CO evolution with a little amount of H_2, affording an accumulated CO of ca. 26.8 μmol with 96.9% CO selectivity, which surpass most reports under the simulated condition in the laboratory. Detailed experimental results disclose that $Ni_2(OH)(PO_4)$ NTs with ultrathin curved walls lead to obvious tensile surface stresses, which makes for the CO_2 photocatalytic process. Then a series of control experiments certify that hydroxyl group anchoring on the surface serving as Lewis base can elevate photocatalytic performance by coordination with CO_2 molecular. So, the synergetic effects with surface-OH and lattice strain enable a substantially enhanced performance for CO_2 photocatalysis. These results not only underline the remarkable CO_2 reduction performance of $Ni_2(OH)(PO_4)$ NTs, but also confirm the possibility of the practical application of photocatalysis in the future.

Acknowledgements

This work was financially supported by the National Natural Science Foundation of China (Nos. 21777046 and 21836002), the National Key Research and Development Program of China (No. 2019YFA0210400), the Guangdong Innovative and Entrepreneurial Research Team Program (No. 2016ZT06N569), the Guangdong Science and Technology Program (No. 2020B121201003), and the Science Technology Project of Guangzhou (No. 201803030002). In addition, we gratefully thank Beijing Synchrotron Radiation Facility at beamline 4W1B for providing us the beam time and discussion.

Electronic Supplementary Material: Supplementary material (SEM, FT-IR, TGA, XPS spectra, Fourier transforms FT ($k^2\chi$ (k)), EXAFS curves-fitting plots, production yield as a function of reaction time, wavelength-dependent of the products generation, photocatalytic test under real sunlight, EIS results, tables of EXAFS fitting results, and Tables of comparison with other catalysts) is available in the online version of this article at https://doi.org/10.1007/s12274-020-3252-4.

References

[1] Lin, R.; Ma, X. L.; Cheong, W. C.; Zhang, C.; Zhu, W.; Pei, J. J.; Zhang, K. Y.; Wang, B.; Liang, S. Y.; Liu, Y. X. et al. PdAg bimetallic electrocatalyst for highly selective reduction of CO_2 with low COOH* formation energy and facile CO desorption. *Nano Res.* **2019**, *12*, 2866–2871.

[2] Chen, W. Y.; Han, B.; Tian, C.; Liu, X. M.; Liang, S. J.; Deng, H.; Lin, Z. MOFs-derived ultrathin holey Co_3O_4 nanosheets for enhanced visible light CO_2 reduction. *Appl. Catal. B* **2019**, *244*, 996–1003.

[3] Liu, L. F.; Zhang, J. L.; Tan, X. N.; Zhang, B. X.; Shi, J. B.; Cheng, X. Y.; Tan, D. X.; Han, B. X.; Zheng, L. R.; Zhang, F. Y. Supercritical CO_2 produces the visible-light-responsive TiO_2/COF heterojunction with enhanced electron-hole separation for high-performance hydrogen evolution. *Nano Res.* **2020**, *13*, 983–988.

[4] Wang, H. P.; Zhang, L.; Wang, K. F.; Sun, X.; Wang, W. Z. Enhanced photocatalytic CO_2 reduction to methane over WO_3·0.33H_2O via Mo doping. *Appl. Catal. B* **2019**, *243*, 771–779.

[5] Han, B.; Ou, X. W.; Deng, Z. Q.; Song, Y.; Tian, C.; Deng, H.; Xu, Y. J.; Lin, Z. Nickel metal–organic framework monolayers for photoreduction of diluted CO_2: Metal-node-dependent activity and selectivity. *Angew. Chem., Int. Ed.* **2018**, *57*, 16811–16815.

[6] Wang, Y.; Huang, N. Y.; Shen, J. Q.; Liao, P. Q.; Chen, X. M.; Zhang, J. P. Hydroxide ligands cooperate with catalytic centers in metal-organic frameworks for efficient photocatalytic CO_2 reduction. *J. Am. Chem. Soc.* **2018**, *140*, 38–41.

[7] Yi, L.; Zhao, W. H.; Huang, Y. H.; Wu, X. Y.; Wang, J. L.; Zhang, G. K. Tungsten bronze $Cs_{0.33}WO_3$ nanorods modified by molybdenum for improved photocatalytic CO_2 reduction directly from air. *Sci. China Mater.* **2020**, *63*, 2206–2214.

[8] Wu, J.; Li, X. D.; Shi, W.; Ling, P. Q.; Sun, Y. F.; Jiao, X. C.; Gao, S.; Liang, L.; Xu, J. Q.; Yan, W. S. et al. Efficient visible-light-driven CO_2 reduction mediated by defect-engineered BiOBr atomic layers. *Angew. Chem., Int. Ed.* **2018**, *130*, 8855–8859.

[9] Chen, S. C.; Wang, H.; Kang, Z. X.; Jin, S.; Zhang, X. D.; Zheng, X. S.; Qi, Z. M.; Zhu, J. F.; Pan, B. C.; Xie, Y. Oxygen vacancy associated single-electron transfer for photofixation of CO_2 to long-chain chemicals. *Nat. Commun.* **2019**, *10*, 788.

[10] Choi, K. M.; Kim, D.; Rungtaweevoranit, B.; Trickett, C. A.; Barmanbek, J. T. D.; Alshammari, A. S.; Yang, P. D.; Yaghi, O. M. Plasmon-enhanced photocatalytic CO_2 conversion within metal–organic frameworks under visible light. *J. Am. Chem. Soc.* **2017**, *139*, 356–362.

[11] Xia, Y.; Cheng, B.; Fan, J. J.; Yu, J. G.; Liu, G. Near-infrared absorbing 2D/3D $ZnIn_2S_4$/N-doped graphene photocatalyst for highly efficient CO_2 capture and photocatalytic reduction. *Sci. China Mater.* **2020**, *63*, 552–565.

[12] You, B.; Tang, M. T.; Tsai, C.; Abild-Pedersen, F.; Zheng, X. L.; Li, H. Enhancing electrocatalytic water splitting by strain engineering. *Adv. Mater.* **2019**, *31*, 1807001.

[13] Xia, Z. H.; Guo, S. J. Strain engineering of metal-based nanomaterials for energy electrocatalysis. *Chem. Soc. Rev.* **2019**, *48*, 3265–3278.

[14] Zhu, H.; Gao, G. H.; Du, M. L.; Zhou, J. H.; Wang, K.; Wu, W. B.; Chen, X.; Li, Y.; Ma, P. M.; Dong, W. F. et al. Atomic-scale core/shell structure engineering induces precise tensile strain to boost hydrogen evolution catalysis. *Adv. Mater.* **2018**, *30*, 1707301.

[15] Wang, L.; Zeng, Z. H.; Gao, W. P.; Maxson, T.; Raciti, D.; Giroux, M.; Pan, X. Q.; Wang, C.; Greeley, J. Tunable intrinsic strain in two-dimensional transition metal electrocatalysts. *Science* **2019**, *363*, 870–874.

[16] Hwang, D. Y.; Choi, K. H.; Park, J. E.; Suh, D. H. Highly efficient hydrogen evolution reaction by strain and phase engineering in composites of Pt and MoS_2 nano-scrolls. *Phys. Chem. Chem. Phys.* **2017**, *19*, 18356–18365.

[17] Ding, F.; Ji, H. X.; Chen, Y. H.; Herklotz, A.; Dörr, K.; Mei, Y. F.; Rastelli, A.; Schmidt, O. G. Stretchable graphene: A close look at fundamental parameters through biaxial straining. *Nano Lett.* **2010**, *10*, 3453–3458.

[18] Ni, B.; Liu, H. L.; Wang, P. P.; He, J.; Wang, X. General synthesis of inorganic single-walled nanotubes. *Nat. Commun.* **2015**, *6*, 8756.

[19] Krasilin, A. A.; Nevedomsky, V. N.; Gusarov, V. V. Comparative energy modeling of multiwalled $Mg_3Si_2O_5(OH)_4$ and $Ni_3Si_2O_5(OH)_4$ nanoscroll growth. *J. Phys. Chem. C* **2017**, *121*, 12495–12502.

[20] Lourenço, M. P.; de Oliveira, C.; Oliveira, A. F.; Guimarães, L.; Duarte, H. A. Structural, electronic, and mechanical properties of single-walled chrysotile nanotube models. *J. Phys. Chem. C* **2012**, *116*, 9405–9411.

[21] Huang, H. W.; Jia, H. H.; Liu, Z.; Gao, P. F.; Zhao, J. T.; Luo, Z. L.; Yang, J. L.; Zeng, J. Understanding of strain effects in the electrochemical reduction of CO_2: Using Pd nanostructures as an ideal platform. *Angew. Chem., Int. Ed.* **2017**, *56*, 3594–3598.

[22] Bian, W.; Huang, Y. C.; Xu, X. B.; Din, M. A. U.; Xie, G.; Wang, X. Iron hydroxide-modified nickel hydroxylphosphate single-wall nanotubes as efficient electrocatalysts for oxygen evolution reactions. *ACS Appl. Mater. Interfaces* **2018**, *10*, 9407–9414.

[23] Ravel, B.; Newville, M. *ATHENA*, *ARTEMIS*, *HEPHAESTUS*: Data analysis for X-ray absorption spectroscopy using *IFEFFIT*. *J. Synchrotron Rad.* **2005**, *12*, 537–541.

[24] Ma, B.; Zhao, J. P.; Ge, Z. H.; Chen, Y. T.; Yuan, Z. H. 5 nm NiCoP nanoparticles coupled with g-C_3N_4 as high-performance photocatalyst for hydrogen evolution. *Sci. China Mater.* **2020**, *63*, 258–266.

[25] Yang, Z. B.; Liang, X. Self-magnetic-attracted $Ni_xFe_{(1-x)}$@$Ni_xFe_{(1-x)}O$ nanoparticles on nickel foam as highly active and stable electrocatalysts towards alkaline oxygen evolution reaction. *Nano Res.* **2020**, *13*, 461–466.

[26] Di, J.; Zhu, C.; Ji, M. X.; Duan, M. L.; Long, R.; Yan, C.; Gu, K. Z.; Xiong, J.; She, Y. B.; Xia, J. X. et al. Defect-rich $Bi_{12}O_{17}Cl_2$ nanotubes self-accelerating charge separation for boosting photocatalytic CO_2 reduction. *Angew. Chem., Int. Ed.* **2018**, *57*, 14847–14851.

[27] Xiong, Y. J.; Ma, Y. N.; Zou, L. L.; Han, S. B.; Chen, H.; Wang, S.; Gu, M.; Shen, Y.; Zhang, L. P.; Xia, Z. H. et al. N-doping induced tensile-strained Pt nanoparticles ensuring an excellent durability of the oxygen reduction reaction. *J. Catal.* **2020**, *382*, 247–255.

[28] Han, B.; Song, J. N.; Liang, S. J.; Chen, W. Y.; Deng, H.; Ou, X. W.; Xu, Y. J.; Lin, Z. Hierarchical $NiCo_2O_4$ hollow nanocages for photoreduction of diluted CO_2: Adsorption and active sites engineering. *Appl. Catal. B* **2020**, *260*, 118208.

[29] Han, B.; Ou, X. W.; Zhong, Z. Q.; Liang, S. J.; Deng, H.; Lin, Z. Rational design of FeNi bimetal modified covalent organic frameworks for photoconversion of anthropogenic CO_2 into widely tunable syngas. *Small* **2020**, *16*, 2002985.

[30] Liang, X.; Wang, X.; Zhuang, J.; Chen, Y.; Wang, D.; Li, Y. Synthesis of nearly monodisperse iron oxide and oxyhydroxide nanocrystals. *Adv. Funct. Mater.* **2006**, *16*, 1805–1813.

[31] Wang, Z. Y.; Jiang, M.; Qin, J. N.; Zhou, H.; Ding, Z. X. Reinforced photocatalytic reduction of CO_2 to CO by a ternary metal oxide $NiCo_2O_4$. *Phys. Chem. Chem. Phys.* **2015**, *17*, 16040–16046.

[32] Wang, S. B.; Guan, B. Y.; Lou, X. W. Rationally designed hierarchical N-doped carbon@$NiCo_2O_4$ double-shelled nanoboxes for enhanced visible light CO_2 reduction. *Energy Environ. Sci.* **2018**, *11*, 306–310.

[33] Wang, Y.; Wang, S. B.; Zhang, S. L.; Lou, X. W. D. Formation of hierarchical $FeCoS_2$-CoS_2 double-shelled nanotubes with enhanced performance for photocatalytic reduction of CO_2. *Angew. Chem., Int. Ed.* **2020**, *132*, 12016–12020.

[34] Chen, W. Y.; Han, B.; Xie, Y. L.; Liang, S. J.; Deng, H.; Lin, Z. Ultrathin Co-Co LDHs nanosheets assembled vertically on MXene: 3D nanoarrays for boosted visible-light-driven CO_2 reduction. *Chem. Eng. J.* **2020**, *391*, 123519.

[35] Tian, S. F.; Chen, S. D.; Ren, X. T.; Hu, Y. Q.; Hu, H. Y.; Sun, J. J.; Bai, F. An efficient visible-light photocatalyst for CO_2 reduction fabricated by cobalt porphyrin and graphitic carbon nitride via covalent bonding. *Nano Res.* **2020**, *13*, 2665–2672.

[36] Li, X. Y.; Rong, H. P.; Zhang, J. T.; Wang, D. S.; Li, Y. D. Modulating the local coordination environment of single-atom catalysts for enhanced catalytic performance. *Nano Res.* **2020**, *13*, 1842–1855.

[37] Gao, C.; Chen, S. M.; Wang, Y.; Wang, J. W.; Zheng, X. S.; Zhu, J. F.; Song, L.; Zhang, W. K.; Xiong, Y. J. Heterogeneous single-atom catalyst for visible-light-driven high-turnover CO_2 reduction: The role of electron transfer. *Adv. Mater.* **2018**, *30*, 1704624.

[38] Li, X. G.; Bi, W. T.; Zhang, L.; Tao, S.; Chu, W. S.; Zhang, Q.; Luo, Y.; Wu, C. Z.; Xie, Y. Single-atom Pt as co-catalyst for enhanced photocatalytic H_2 evolution. *Adv. Mater.* **2016**, *28*, 2427–2431.

[39] Leng, F. C.; Liu, H.; Ding, M. L.; Lin, Q. P.; Jiang, H. L. Boosting photocatalytic hydrogen production of porphyrinic MOFs: The metal location in metalloporphyrin matters. *ACS Catal.* **2018**, *8*, 4583–4590.

[40] Huang, L. X.; Han, B.; Huang, X. H.; Liang, S. J.; Deng, Z. Q.; Chen, W. Y.; Peng, M.; Deng, H. Ultrathin 2D/2D $ZnIn_2S_4$/MoS_2 hybrids for boosted photocatalytic hydrogen evolution under visible light. *J. Alloys Compd.* **2019**, *798*, 553–559.

[41] Li, Q.; Wang, S. C.; Sun, Z. X.; Tang, Q. J.; Liu, Y. Q.; Wang, L. Z.; Wang, H. Q.; Wu, Z. B. Enhanced CH_4 selectivity in CO_2 photocatalytic reduction over carbon quantum dots decorated and oxygen doping g-C_3N_4. *Nano Res.* **2019**, *12*, 2749–2759.

[42] Li, P.; Liu, W.; Dennis, J. S.; Zeng, H. C. Synthetic architecture of MgO/C nanocomposite from hierarchical-structured coordination polymer toward enhanced CO_2 capture. *ACS Appl. Mater. Interfaces* **2017**, *9*, 9592–9602.

[43] Zhang, Y. Z.; Xia, B. Q.; Ran, J. R.; Davey, K.; Qiao, S. Z. Atomic-level reactive sites for semiconductor-based photocatalytic CO_2 reduction. *Adv. Energy Mater.* **2020**, *10*, 1903879.

[44] Liu, B.; Li, C. M.; Zhang, G. Q.; Yao, X. S.; Chuang, S. S. C.; Li, Z. Oxygen vacancy promoting dimethyl carbonate synthesis from CO_2 and methanol over Zr-doped CeO_2 nanorods. *ACS Catal.* **2018**, *8*, 10446–10456.

[45] Torres, J. A.; Nogueira, A. E.; da Silva, G. T. S. T.; Lopes, O. F.; Wang, Y. J.; He, T.; Ribeiro, C. Enhancing TiO_2 activity for CO_2 photoreduction through MgO decoration. *J. CO_2 Util.* **2020**, *35*, 106–114.

[46] Meng, X. G.; Ouyang, S. X.; Kako, T.; Li, P.; Yu, Q.; Wang, T.; Ye, J. H. Photocatalytic CO_2 conversion over alkali modified TiO_2 without loading noble metal cocatalyst. *Chem. Commun.* **2014**, *50*, 11517–11519.

[47] Yang, Y.; Wu, J. J.; Xiao, T. T.; Tang, Z.; Shen, J. Y.; Li, H. J.; Zhou, Y.; Zou, Z. G. Urchin-like hierarchical CoZnAl-LDH/RGO/g-C_3N_4 hybrid as a Z-scheme photocatalyst for efficient and selective CO_2 reduction. *Appl. Catal. B* **2019**, *255*, 117771.

[48] Chen, Y. Z.; Li, H. L.; Zhao, W. H.; Zhang, W. B.; Li, J. W.; Li, W.; Zheng, X. S.; Yan, W. S.; Zhang, W. H.; Zhu, J. F. et al. Optimizing reaction paths for methanol synthesis from CO_2 hydrogenation via metal-ligand cooperativity. *Nat. Commun.* **2019**, *10*, 1885.

[49] Dong, Y. C.; Ghuman, K. K.; Popescu, R.; Duchesne, P. N.; Zhou, W. J.; Loh, J. Y. Y.; Jelle, A. A.; Jia, J.; Wang, D.; Mu, X. K. et al. Tailoring surface frustrated Lewis pairs of $In_2O_{3-x}(OH)_y$ for gas-phase heterogeneous photocatalytic reduction of CO_2 by isomorphous substitution of In^{3+} with Bi^{3+}. *Adv*. *Sci*. **2018**, *5*, 1700732.

[50] Zhu, W.; Zhang, C. F.; Li, Q.; Xiong, L. K.; Chen, R. X.; Wan, X. B.; Wang, Z.; Chen, W.; Deng, Z.; Peng, Y. Selective reduction of CO_2 by conductive MOF nanosheets as an efficient co-catalyst under visible light illumination. *Appl*. *Catal*. *B* **2018**, *238*, 339–345.

[51] Petrie, J. R.; Jeen, H.; Barron, S. C.; Meyer, T. L.; Lee, H. N. Enhancing perovskite electrocatalysis through strain tuning of the oxygen deficiency. *J*. *Am*. *Chem*. *Soc*. **2016**, *138*, 7252–7255.

[52] Jansonius, R. P.; Reid, L. M.; Virca, C. N.; Berlinguette, C. P. Strain engineering electrocatalysts for selective CO_2 reduction. *ACS Energy Lett*. **2019**, *4*, 980–986.

[53] Chen, W. Y.; Liu, X. M.; Han, B.; Liang, S. J.; Deng, H.; Lin, Z. Boosted photoreduction of diluted CO_2 through oxygen vacancy engineering in NiO nanoplatelets. *Nano Res*. in press, DOI: 10.1007/s12274-020-3105-1.